Electrostatic effects and topological superconductivity in semiconductor–superconductor–magnetic-insulator hybrid wires

Benjamin D. Woods and Tudor D. Stanescu
Department of Physics and Astronomy, West Virginia University, Morgantown, West Virginia 26506, USA

(Received 13 November 2020; revised 16 November 2021; accepted 17 November 2021; published 29 November 2021)

We investigate the impact of electrostatics on the proximity effect between a magnetic insulator and a semiconductor wire in semiconductor–superconductor–magnetic-insulator hybrid structures. By performing self-consistent Schrödinger-Poisson calculations using an effective model of the hybrid system, we find that large effective Zeeman fields consistent with the emergence of topological superconductivity emerge within a large parameter window in wires with overlapping layers of magnetic insulator and superconductor, but not in nonoverlapping structures. We show that this behavior is essentially the result of electrostatic effects controlling the amplitude of the low-energy wave functions near the semiconductor–magnetic-insulator interface.

DOI: 10.1103/PhysRevB.104.195433

I. INTRODUCTION

The successful experimental realization of Majorana zero modes (MZMs)—non-Abelian anyons [1] representing the condensed-matter analogs of Majorana fermions [2,3] that provide a promising platform for topological quantum computing [4–7]—depends critically on the robustness of the topological superconducting phase that hosts them [8–14]. In the absence of naturally occurring one-dimensional topological superconductors, the research has focused on hybrid structures [15–17], particularly semiconductor (SM) wires proximity coupled to *s*-wave superconductors (SCs) in the presence of a magnetic field parallel to the wire [18–24]. A large enough field-induced Zeeman splitting ensures the emergence of a topological superconducting phase, even in the presence of some weak/moderate system inhomogeneity. However, in addition to suppressing the gap of the parent superconductor, in which orbital effects play an important role [25] and which severely limits the realization of robust topological superconductivity, the applied magnetic field imposes serious constraints on the possible device layout for Majorana-based topological qubits [26].

A possible solution is to create the required Zeeman field by proximity coupling the semiconductor to a magnetic insulator [16,27]. Recently, this possibility has been explored experimentally using InAs nanowires with epitaxial layers of superconducting Al and ferromagnetic EuS [28–30]. A key finding was that an effective Zeeman field $\Gamma_{\rm eff}^{\rm SC}$ of order 1 T ($\sim$0.05 meV) emerges in the superconductor in the absence of an applied magnetic field, but only in nanowires with *overlapping* shells of superconductor and ferromagnetic insulator [28]. Correlated with the emergence of an effective Zeeman field in the superconductor was the observation of zero-bias conductance peaks for charge tunneling into the end of the semiconductor wire, which is consistent with the presence of topological superconductivity. These features are absent in hybrid structures with *nonoverlapping* Al and EuS covered facets [28].

The crucial question concerns the physical mechanism responsible for the startling contrast between the phenomenologies observed in the two setups. Furthermore, one may ask if, based on the understanding of this mechanism, one can identify efficient knobs for controlling the magnitude of the effective Zeeman field emerging in the nanowire, to ensure that the topological superconducting phase is accessible and robust.

A natural candidate for explaining the difference between the behaviors associated with the two setups is the ferromagnetic exchange coupling occurring inside the SC in the overlapping geometry due to spin-dependent scattering at the Al-EuS interface [31–35]. In turn, the proximity effect generated by the exchange-coupled superconductor inside the spin-orbit coupled nanowire could lead to the emergence of a topological superconducting state. In this scenario, the effective Zeeman field $\Gamma_{\rm eff}^{\rm SM}$ required to drive the SM nanowire into the topological regime is induced "indirectly," via the Al layer. Consequently, it is controlled by the strength $\widetilde{\gamma}$ of the effective coupling between the semiconductor and superconductor, which also determines the size of the induced superconducting gap and the critical Zeeman field associated with the topological quantum phase transition (TQPT) [36]. In particular, the minimum value of the critical field is given by $\widetilde{\gamma}$, and it can be significantly larger than the induced gap in the strong-coupling limit [36]. This poses a serious problem for the "mediated proximity" scenario. As explicitly shown below, the topological condition $\Gamma_{\rm eff}^{\rm SM} > \widetilde{\gamma}$ is inconsistent with the experimental parameters reported in Ref. [28] and, more importantly, is generally inconsistent with robust topological superconductivity.

In this paper, we investigate a different scenario involving the "direct" proximity effect at the semiconductor–magnetic-insulator (SM-MI) interface. We show that the strength of the effective Zeeman field $\Gamma_{\rm eff}^{\rm SM}$ induced in the wire by proximity to the MI is controlled by electrostatic effects, which, in turn, depend on the geometry of the SC layer and on the applied gate potential. In essence, because of the finite

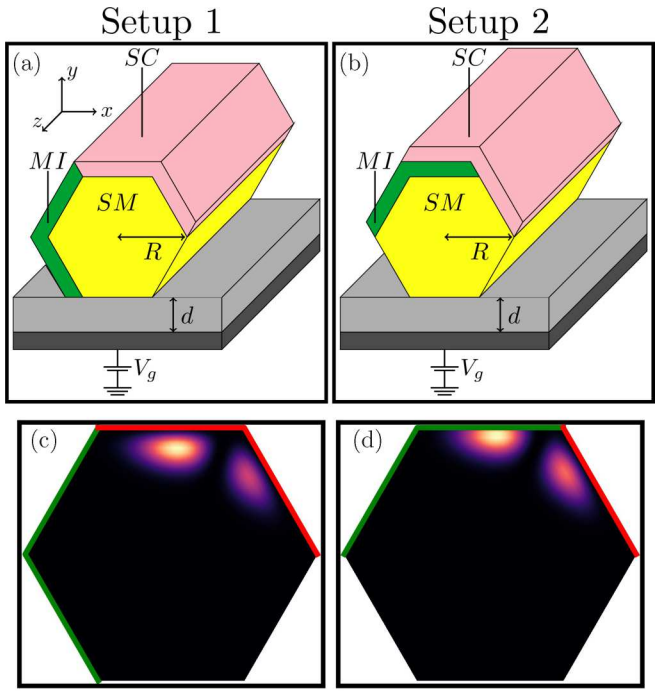

FIG. 1. Top panels: Schematic representation of the hybrid structure studied in this work corresponding to a semiconductor nanowire (yellow) with (a) nonoverlapping (setup 1) and (b) overlapping (setup 2) layers of superconductor (pink) and magnetic insulator (green). An external potential is applied using a back-gate (black) separated from the wire by an insulating dielectric layer (gray). Parameters: $R = 50$ nm, $d = 10$ nm. Bottom panels: Wave-function profile of the second lowest transverse mode for parameters corresponding to this mode being near the Fermi level: $V_g \approx -1.1$ V, $V_{\rm SC} = 0.15$ V.

work-function difference between the SM wire and the SC shell, the wave functions characterizing the low-energy states in the wire are strongly "attracted" toward the superconductor, regardless of whether the SM and SC are in direct contact or separated by a MI layer. This means away from the SM-MI interface in the nonoverlapping setup and toward the SM-MI interface in the system with overlapping MI and SC layers (see Fig. 1). As a result, the induced $\Gamma_{\rm eff}^{\rm SM}$ has significantly higher values in the overlapping structure as compared to the nonoverlapping setup. By performing self-consistent Schrödinger-Poisson calculations, we demonstrate that the overlapping setup is consistent with the emergence of topological superconductivity over a large window of system parameters and applied gate potentials, in sharp contrast with the nonoverlapping structure. Our findings support the feasibility of topological superconductivity in SM-SC-MI hybrid structures, and they provide guidance for controlling the system and enhancing the robustness of the topological phase.

II. MEDIATED PROXIMITY SCENARIO

Before we present our model calculations, let us briefly discuss the "mediated proximity" scenario. In the strong-coupling limit, satisfying the topological condition $\Gamma_{\rm eff}^{\rm SM} > \widetilde{\gamma}$ requires a large effective Zeeman field $\Gamma_{\rm eff}^{\rm SC}$ inside the SC, possibly exceeding the Chandrasekhar-Clogston (CC) limit [37,38]. Even assuming that spin-orbit coupling induced by proximity to the SM wire prevents the closing of the SC gap, its value (and, implicitly, the size of the topological gap) will be very small. On the other hand, in the weak/intermediate regime, the induced SC gap and effective Zeeman field are approximately given by [36]

$$\Delta_{\rm ind} \approx \frac{\widetilde{\gamma}\,\Delta}{\widetilde{\gamma}+\Delta}, \qquad \Gamma_{\rm eff}^{\rm SM} \approx \frac{\widetilde{\gamma}\,\Gamma_{\rm eff}^{\rm SC}}{\widetilde{\gamma}+\Delta}, \tag{1}$$

where Δ is the order parameter of the SC, and $\widetilde{\gamma}$ is the effective coupling between the SC and the SM subband of interest. The factor $\widetilde{\gamma}/(\Delta+\widetilde{\gamma})$ in Eq. (1) accounts for the renormalization effects of the SC on the SM. Note that Δ is reduced from its zero Zeeman field value by the presence of the ferromagnetic insulator, which we assume to already be taken into account for Δ throughout this section. Satisfying the topological condition requires [36]

$$\Gamma_{\rm eff}^{\rm SM} > \widetilde{\gamma} \tag{2}$$

in the limit of vanishing chemical potential, $\mu = 0$, with respect to the bottom of an SM subband. Note that this is different from the often cited expression for the topological condition, $\Gamma_{\rm eff}^{\rm SM} > \Delta_{\rm ind}$, due to the renormalization effects of the SC. Combining Eqs. (1) and (2) yields

$$\Gamma_{\rm eff}^{\rm SC} > \frac{\Delta^2}{\Delta-\Delta_{\rm ind}} \geqslant \Delta. \tag{3}$$

First, we note that the parameters characterizing the recent experiment [28], i.e., $\Gamma_{\rm eff}^{\rm SC} \sim \Delta_{\rm ind} \sim 0.05$ meV, do not satisfy Eq. (3). Second, note that the CC limit restricts the Zeeman field to [37,38]

$$\Gamma_{\rm eff}^{\rm SC} \leqslant \frac{\Delta}{\sqrt{2}} \tag{4}$$

in order for the superconducting state to survive. Clearly, Eqs. (3) and (4) cannot be satisfied simultaneously. This leads to the conclusion that the "mediated proximity" mechanism does not enable the realization of robust topological superconductivity in SM-SC-MI hybrid structures, and it suggests that the investigation of the "direct" proximity effect at the SM-MI interface is critical for understanding the low-energy physics in these systems.

III. MODEL

The SM-SC-MI hybrid system studied in this section is represented schematically in the top panels of Fig. 1. We focus on two setups corresponding to the nonoverlapping (setup 1 in Fig. 1) and overlapping (setup 2) configurations investigated in the recent experiment [28]. We do not address explicitly the proximity effect between the MI and the SC (in setup 2), but we focus instead on the impact of electrostatics on the proximity-induced Zeeman field and pairing potential at the SM-MI and SM-SC interfaces, respectively. The SM-SC-MI hybrid system, assumed to be infinitely long, is described by the Hamiltonian

$$H(k_z) = H_o(k_z) + H_b. \tag{5}$$

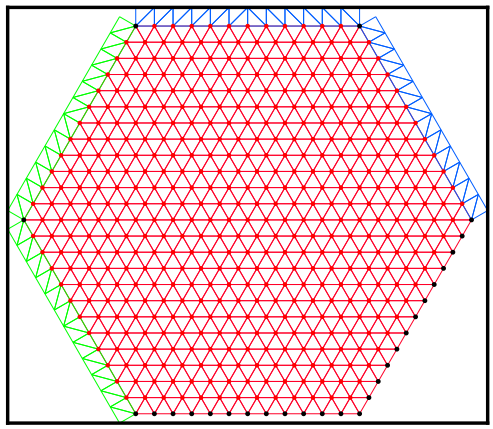

FIG. 2. Finite-element mesh used for simulation of setup 1 of Fig. 1. A basis function is associated with each vertex in the mesh. The SM region is shown in red. A single layer of the MI and SC meshes is shown in green and blue, respectively. The rest of the MI and SC regions extend to infinity by repeating the shown single layers, but the degrees of freedom from these regions are integrated out. The spacing between vertices is exaggerated in this figure for clarity. In the actual simulation mesh, the vertex spacing in the SM is 2 nm, while in the MI and SC regions the vertex spacing is 0.01 nm.

The first term, which includes the SM wire and the SC and MI layers, is given by

$$H_o(k_z) = \Bigg[-\nabla_\perp \cdot \frac{\hbar^2}{2m^*(\mathbf{r}_\perp)}\nabla_\perp + \frac{\hbar^2 k_z^2}{2m^*(\mathbf{r}_\perp)} - \mu(\mathbf{r}_\perp) - e\phi(\mathbf{r}_\perp) + \Gamma(\mathbf{r}_\perp)\sigma_z + \alpha(\mathbf{r}_\perp)k_z\sigma_y\Bigg]\tau_z + \Delta(\mathbf{r}_\perp)\sigma_y\tau_y, \tag{6}$$

where m^* is the subsystem-dependent effective mass, $\nabla_\perp$ and $\mathbf{r}_\perp$ are the gradient and position operators in the xy-plane (i.e., transverse to the wire axis), respectively, μ is the chemical potential, ϕ is the electrostatic potential, Γ is the Zeeman energy, α is the Rashba spin-orbit coefficient, Δ is the superconducting pairing, k_z is the Bloch wave number along the length of the wire, and σ_i and τ_i are Pauli matrices acting in spin and particle-hole space, respectively. Note that these parameters are piecewise functions with respect to the SM, SC, and MI regions. In particular, α, Δ, and Γ are uniform and nonzero only within the SM, SC, and MI regions, respectively. Each region, therefore, provides a necessary ingredient for topological superconductivity, as captured by, e.g., the minimal 1D models [18,19]. For simplicity, we have neglected transverse spin-orbit coupling. The three regions are characterized by different effective masses and chemical potential values (relative to the bottom of the corresponding bands). Specifically, we have $m^*_{\mathrm{SM}} = 0.023m_o$, $m^*_{\mathrm{SC}} = m_o$, $m^*_{\mathrm{MI}} = m_o$ [39] (where m_o is the free-electron mass), $\mu_{\mathrm{SM}} = 0$, $\mu_{\mathrm{SC}} = 10$ eV, and $\mu_{\mathrm{MI}} = -1$ eV [29].

We model the SC region of the device as a semi-infinite bulk superconductor, which avoids including disorder as an ingredient needed to reproduce the experimentally observed induced gaps [40] for systems with thin superconductor layers. As shown in Fig. 2, a bulk superconducting region is attached to each facet of the SM which is in direct contact with the SC. Note that we do not attach a bulk superconducting region to the top of the MI region in setup 2 [see Fig. 1(b)], since we are not considering the direct proximity effects between the MI and SC regions. To control the coupling between the SM and bulk SC(s), we include a barrier potential at the SM-SC interface,

$$H_b = V_b \sum_n \delta(u_n - \sqrt{3}R/2)\tau_z, \tag{7}$$

where V_b is the barrier strength, δ is the Dirac delta function, the sum runs over all SM-SC interfaces, and u_n is the coordinate normal to the nth SM-SC interface.

Similarly, we also model the MI as a bulk magnetic insulator by attaching a bulk MI region to each facet of the SM which is in direct contact with the MI (see Fig. 2). Note that the wave function exponentially decays into the MI due to the large negative chemical potential μ_{MI} of the MI. The decay length is extremely small (<1 nm), so even a MI layer of a few nm's behaves essentially identical to a semi-infinite MI region. Note that inclusion of semi-infinite bulk SC and MI regions inhibits us from performing a straightforward, brute-force numerical calculation in which the SC and MI degrees of freedom are included in a finite-dimensional Hamiltonian matrix. To overcome this issue, we employ a Green's function approach in which the degrees of freedom of the bulk SC and MI regions are integrated out and included as a self-energy. After integrating out the MI and SC degrees of freedom, the SM wire is described by the energy-dependent effective "Hamiltonian,"

$$H_{\mathrm{eff}}(k_z, \omega) = H_{\mathrm{SM}}(k_z) + \Sigma_{\mathrm{MI}}(k_z, \omega) + \Sigma_{\mathrm{SC}}(k_z, \omega), \tag{8}$$

where k_z is the wave number along the wire axis, H_{SM} is the bare SM Hamiltonian, and Σ_{MI} and Σ_{SC} are self-energies characterizing the proximity effects at the SM-MI and SM-SC interfaces, respectively. Details regarding the self-energy method are provided in the Appendix.

Finally, the electrostatic potential ϕ is governed by the Poisson equation,

$$-\nabla_\perp \cdot \varepsilon(\mathbf{r}_\perp)\nabla_\perp\phi(\mathbf{r}_\perp) = \rho(\mathbf{r}_\perp), \tag{9}$$

where ε is the region-dependent permittivity, and ρ is the charge density. The relative permittivity of the SM, MI, dielectric, and surrounding air are given by 15.2, 11.1, 24, and 1, respectively. The potential is subject to Dirichlet boundary conditions on the back-gate, V_g, and superconductor, V_{SC}, which accounts for band-bending at the SM-SC interface. In addition, we impose von Neumann–type boundary conditions on the top, left, and right surfaces of a box of side length b surrounding the wire. We emphasize that the potential within the nanowire is negligibly affected by these boundary conditions—e.g., the exact value of b or whether we choose von Neumann or Dirichlet boundary conditions on the top, left, and right surfaces of the box—provided $b \gg R$. The charge density in (9) is determined by the occupied states of the Hamiltonian (5), which in turn depend upon the electrostatic potential, ϕ. Therefore, Eqs. (5) and (9) represent a coupled set of Schrödinger-Poisson equations requiring a self-consistent solution for the charge density and electrostatic potential [41]. Solving the Schrödinger-Poisson equations in

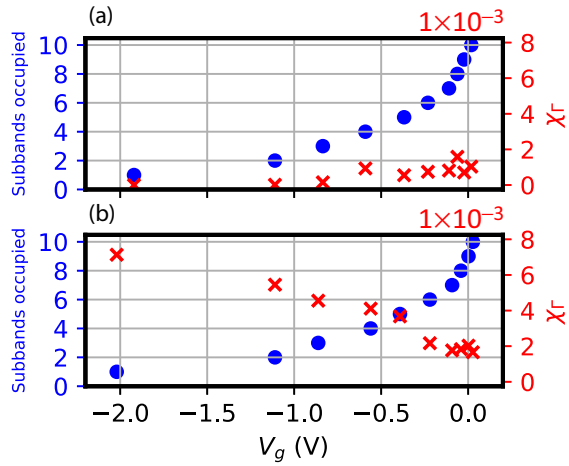

FIG. 3. Blue disks: Subband occupancy as a function of the applied gate potential V_g for (a) setup 1 and (b) setup 2. The values of V_g correspond to the bottom of a certain subband n being at the chemical potential. Note the negligible difference between the two setups. Red crosses: Linear susceptibility $\chi_{\Gamma,n} = \Gamma^{\rm SM}_{{\rm eff},n}/\Gamma$ characterizing the direct proximity effect at the SM-MI interface. Note the significant difference between (a) setup 1 and (b) setup 2, indicative of a much stronger direct SM-MI proximity effect in the overlapping configuration as compared to the nonoverlapping setup. The system parameters are $V_b \to \infty$, $\Gamma \to 0$, and $V_{\rm SC} = 0.15$ V.

the presence of the bulk superconductor is a nontrivial task due to the continuum of states with energies outside of the superconducting gap. We therefore work in the limit of $V_b \to \infty$ (e.g., the SC is uncoupled from the SM and MI regions within the Hamiltonian) when solving for the electrostatic potential, ϕ, self-consistently. The resulting potential is then used in the Hamiltonian for noninfinite V_b. Note that the presence of the superconductor still plays a key role in determining the potential since it provides a boundary condition for the Poisson equation.

The eigenstates of the Hamiltonian (8) are found using finite-element methods [42,43]. A linear Lagrange basis set is used on a structured triangular mesh with 2 nm between vertices within the SM region as shown in Fig. 2. The mesh within the MI and SC regions has a much smaller vertex spacing of 0.01 nm in the direction normal to the SM-MI and SM-SC interfaces to handle the large effective masses of these regions. The finite-element package FEniCS [44] is used when solving the Poisson equation (9). Meshes for the Poisson equation are generated using Gmsh [45] with characteristic vertex spacings within the SM, MI, dielectric, and surrounding air chosen to be 1.5, 1, 2, and 10 nm, respectively.

IV. RESULTS

First, we determine the dependence of the number of occupied subbands on the applied gate potential (V_g) and identify the values of V_g corresponding to the bottom of a certain subband n being at the chemical potential, which provides the optimal condition for the emergence of topological superconductivity. The results are shown in Fig. 3 (blue disks). Note that the differences in subband occupancy between setups 1 and 2 are very small, which demonstrates that electrostatic effects depend weakly on the location of the magnetic insulator layer. Next, we solve the equation $H_{\rm eff}\psi = \omega\psi$ corresponding to $V_b \to \infty$ and $\Gamma \to 0$ and calculate the (linear) susceptibility $\chi_{\Gamma,n} = \Gamma^{\rm SM}_{{\rm eff},n}/\Gamma$ characterizing the direct proximity effect at the SM-MI interface. Here, $\Gamma^{\rm SM}_{{\rm eff},n} = \frac{1}{2}(E_{n,\uparrow} - E_{n,\downarrow})$, where $E_{n,\uparrow}$ and $E_{n,\downarrow}$ are the energies of the spin-up and spin-down eigenstates of the nth SM subband for $k_z = 0$ and $V_b \to \infty$. The results are shown in Fig. 3 (red crosses). Note the striking difference between the two setups. Particularly significant is that in the low-occupancy regime $n \lesssim 5$, which is expected to be most favorable for realizing robust topological superconductivity [46], the susceptibility for setup 2 (overlapping layers) is 5–50 times higher than the corresponding susceptibility for setup 1. This behavior is determined by electrostatic effects, which result in the wave function of the lowest-energy mode (relative to the Fermi level) being localized in the vicinity of the superconductor, as shown, for example, in Figs. 1(c) and 1(d). For setup 1, this implies a wave function localized away from the SM-MI interface (hence, weak SM-MI proximity effect), while for setup 2 the wave function has a significant amplitude at the interface with the magnetic insulator, leading to large values of χ_Γ. We note that the wave functions associated with higher energy transverse modes are more delocalized, reducing the difference between the two setups. However, the high-occupancy regime is characterized by a small intersubband spacing, which makes the topological phase susceptible to disorder and other types of system inhomogeneity [46].

Having elucidated the key role played by electrostatics in determining the strength of the SM-MI proximity effect, we calculate the topological phase diagram as a function of the bare Zeeman field Γ and the applied gate voltage V_g for a hybrid system with $\Delta_o = 0.3$ meV [47] and a SM-SC interface barrier $V_b = 2.75$ eV nm. The phase boundary separating the trivial and topological superconducting phases is obtained by finding Γ such that the equation $H_{\rm eff}(k_z = 0, \omega = 0)\psi = 0$ is satisfied. The results are shown in Fig. 4. Note that the overlapping configuration (setup 2) is consistent with the emergence of a topological phase for $\Gamma \sim 100$–200 meV and V_g near the optimal values corresponding to the bottom of a certain subband being at the Fermi level [see Fig. 4(a)]. By contrast, the nonoverlapping structure (setup 1) cannot support topological superconductivity for $\Gamma < 500$ meV, except in the high-occupancy regime [see Figs. 4(b) and 4(c)]. We emphasize that including the "indirect" proximity effect for setup 2 reduces the parent SC gap Δ and generates an effective Zeeman field $\Gamma^{\rm SC}_{\rm eff}$ inside the parent superconductor, which favors the emergence of topological superconductivity and further enhances the already substantial difference between the two setups.

To demonstrate the robustness of our results, we investigate the dependence of the minimum critical field $\Gamma^n_{c,\rm min}$ characterizing the topological phase transition associated with subband n on the strength of the effective SM-SC coupling $\widetilde{\gamma}$ for two values of the SM-SC work-function difference $V_{\rm SC}$. The effective coupling is calculated from Eq. (1) as $\widetilde{\gamma} = \Delta_{\rm ind}\sqrt{\Delta_o + \Delta_{\rm ind}}/\sqrt{\Delta_o - \Delta_{\rm ind}}$ [36], where $\Delta_{\rm ind}$ is the induced gap for $\Gamma^{\rm SM}_{\rm eff} = 0$. The results shown in Fig. 5 confirm the striking difference between the overlapping (dashed lines) and the nonoverlapping (solid lines) setups. More specifically, the

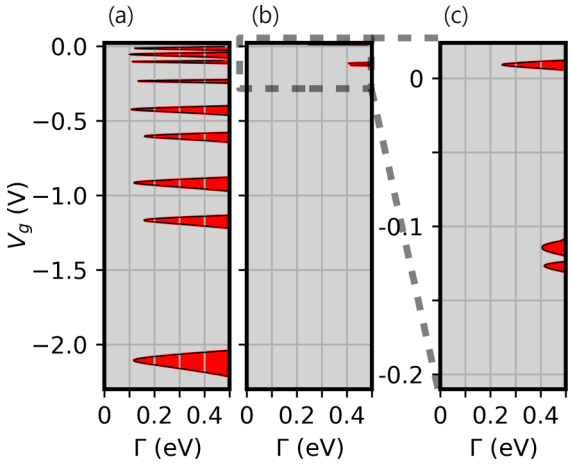

FIG. 4. Topological phase diagram as a function of the (phenomenological) Zeeman field Γ characterizing the MI and the applied gate potential V_g for (a) the overlapping structure (setup 2) and (b) the nonoverlapping structure (setup 1). Panel (c) is an inset corresponding to the high-occupancy regime in panel (b). Note that setup 2 is consistent with the emergence of topological superconductivity within a significant parameter window, in sharp contrast with setup 1. The system parameters are $V_{SC} = 0.15$ V and $V_b = 2.75$ eV nm.

(bare) minimum critical Zeeman fields required for the emergence of a topological SC phase are systematically larger (by up to three orders of magnitude) in the nonoverlapping configurations as compared to the overlapping setup. A comparison between panels (a) and (b) in Fig. 5 shows that this trend increases with V_{SC}. Including the "indirect" proximity effect can only enhance the difference between the two configurations. Note that the spin splitting in EuS, $\Gamma \approx 0.14$–0.19 eV near the zone center [48], is consistent with the emergence (in overlapping structures, within a significant $\tilde{\gamma}$ range) of topological SC induced by the "direct" proximity effect (alone).

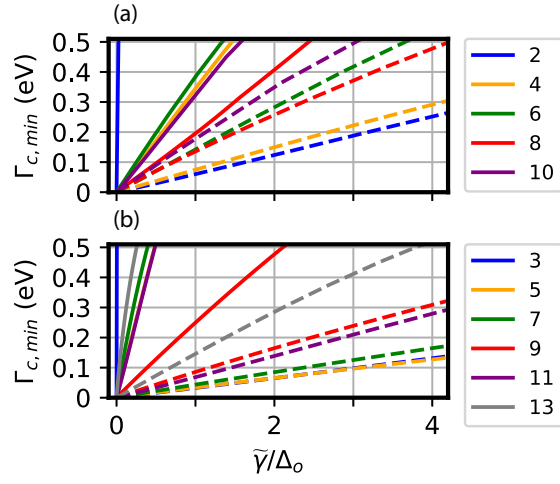

FIG. 5. Dependence of the minimum critical Zeeman field $\Gamma^n_{c,\min}$ on the effective SM-SC coupling $\tilde{\gamma}$ for two values of the SM-SC work-function difference: (a) $V_{SC} = 0.15$ V and (b) $V_{SC} = 0.3$ V. The full lines correspond to setup 1, while the dashed lines are for the overlapping structure (setup 2). Note that the minimum critical Zeeman fields required for the emergence of a topological SC phase are systematically larger (by up to three orders of magnitude) in the nonoverlapping configuration as compared to the overlapping setup.

V. CONCLUSION

In conclusion, we have demonstrated that electrostatic effects play a critical role in determining the strength of the (direct) proximity effect between a magnetic insulator and a semiconductor wire in semiconductor–superconductor–magnetic-insulator (SM-SC-MI) hybrid structures. This decisive impact of electrostatics is rather generic in proximity-coupled hybrid nanostructures, beyond the SM-SC-MI system discussed as a specific example. Here, the electrostatic effects are controlled by the applied gate potential and by the geometry of the superconducting layer, regardless of whether the SM and SC are in direct contact or separated by a MI layer. We have argued that the "indirect" proximity effect emerging in structures with overlapping SC and MI layers is generally insufficient for the realization of a topological superconducting phase in the hybrid system. However, in these overlapping structures, electrostatics favors the realization of low-energy transverse modes with large amplitudes near the SM-MI interface, which, in turn, results in a strong proximity effect between the MI and the SM wire and the emergence of a large effective Zeeman field consistent with the presence of topological superconductivity. By contrast, such large proximity-induced Zeeman fields do not occur in nonoverlapping structures within similar parameter windows. On the one hand, our results suggest that the recently reported experimental findings [28] are consistent with the presence of small proximity-induced Zeeman fields and topologically trivial superconductivity in nonoverlapping structures and significant effective Zeeman fields in the overlapping setup, large enough to generate topological superconductivity in a homogeneous system. On the other hand, our findings suggest possible strategies for enhancing the robustness of the topological superconducting phase realized in a SM-SC-MI hybrid system. For example, using a lateral gate (instead of or in addition to a back gate) may enable a better control of the amplitudes of the relevant wave functions at the interfaces between the SM wire and the magnetic insulator or the parent superconductor. In addition, changing the areas of the SM-SC and SC-MI interfaces (e.g., having three facets covered by superconductor) can significantly affect the strength of the induced SC pairing potential and effective Zeeman field. Finally, since the "indirect" proximity effect alone cannot generate topological superconductivity and is not required to generate it, as shown in this study, but has the rather undesired effect of reducing the superconducting order parameter of the parent SC, it may be convenient to reduce the effective coupling at the SC-MI interface, e.g., by adding a thin nonmagnetic insulating layer. This would have a minimal impact on the electrostatics, while enhancing the induced SC gap. Of course, quantitative estimates of the topological gap within these scenarios require a more detailed modeling of the hybrid structure that explicitly includes the proximity effect at the SC-MI interface.

ACKNOWLEDGMENT

This work is supported by NSF Grant No. 2014156.

APPENDIX: GREEN'S FUNCTION METHOD

As stated in Sec. III of the main text, inclusion of semi-infinite bulk SC and MI regions inhibits us from performing a straightforward, brute-force numerical calculation in which the SC and MI degrees of freedom are included in a finite-dimensional Hamiltonian matrix. To overcome this issue, we employ a Green's function approach in which the degrees of freedom of the bulk SC and MI regions are integrated out and included as a self-energy. The Green's function restricted to the SM is given by

$$G_{\mathrm{SM}}(k_z,\omega,\Gamma) = (\omega S_{\mathrm{SM}} - H_{\mathrm{SM}}(k_z) - \Sigma_{\mathrm{MI}}(k_z,\omega,\Gamma) - \Sigma_{\mathrm{SC}}(k_z,\omega))^{-1}, \quad \text{(A1)}$$

where H_{SM} is the matrix representation of the Hamiltonian (5) restricted to the SM region (red region in Fig. 2), Σ_{MI} and Σ_{SC} are the momentum- and energy-dependent self-energies due to the MI and SC semi-infinite regions, respectively, and S_{SM} is the overlap matrix whose elements are the overlap of the SM basis functions. The self-energies are computed using the surface Green's functions of the semi-infinite regions, which are calculated using the accelerated iterative algorithm of Refs. [49,50]. The MI self-energy is only weakly dependent on k_z and ω over the relevant inverse length and energy scales of the problem due to the large effective mass m^*_{MI} and the large negative chemical potential μ_{MI} of the MI. It can therefore be well approximated by simply ignoring such dependencies. We approximate the MI self-energy as

$$\Sigma_{\mathrm{MI}}(k_z,\omega,\Gamma) \to \Sigma_{\mathrm{MI}}(0,0,\Gamma) = \Sigma^{\mathrm{static}}_{\mathrm{MI}}(\Gamma). \quad \text{(A2)}$$

As stated in the main text, solving the Schrödinger-Poisson equations in the presence of the bulk superconductor is a nontrivial task due to the continuum of states with energies outside of the superconducting gap. We therefore work in the limit of $V_b \to \infty$ (e.g., the SC is uncoupled from the SM and MI regions within the Hamiltonian) when solving for the electrostatic potential, ϕ, self-consistently. The relevant effective Hamiltonian is then

$$H^{\phi}_{\mathrm{eff}}(k_z,\Gamma) = H_{\mathrm{SM}}(k_z) + \Sigma^{\mathrm{static}}_{\mathrm{MI}}(\Gamma), \quad \text{(A3)}$$

where we have used the superscript ϕ to indicate that this effective Hamiltonian is used only for solving for ϕ self-consistently. Importantly, this effective Hamiltonian is energy-independent due to the static approximation of the MI self-energy, which allows for efficient self-consistent calculation of ϕ [41].

Eigenstates of the full Hamiltonian (including the bulk SC) are indicated by the poles of the Green's function (A1). We are particularly interested in finding zero-energy states, since they indicate topological phase transitions. This is equivalent to finding the zero-energy states of another effective, energy-independent Hamiltonian,

$$H^{\mathrm{top}}_{\mathrm{eff}}(k_z,\Gamma) = H_{\mathrm{SM}}(k_z) + \Sigma^{\mathrm{static}}_{\mathrm{MI}}(\Gamma) + \Sigma_{\mathrm{SC}}(k_z,0), \quad \text{(A4)}$$

where the zero-energy SC self-energy is used. This effective Hamiltonian completely describes the system with respect to calculating the topological phase diagram. Note that we have used the superscript "top" to indicate that this effective Hamiltonian is used solely to calculate the topological phase diagram. Importantly, the effective Hamiltonian (A4) lends itself to numerical calculations since it only contains the finite number of SM degrees of freedom. We are also interested in calculating the induced superconducting gap with $\Gamma = 0$ to assess the coupling strength between the SM and SC. To do so, we need to calculate subgap states, i.e., states below the superconducting gap of the parent superconductor. Both of the self-energies in (A1) are purely real within the superconducting gap of the parent superconductor, implying that any subgap states must satisfy the generalized eigenvalue equation,

$$H^{\mathrm{ind}}_{\mathrm{eff}}(k_z,\omega)\psi(k_z) = \omega S_{\mathrm{SM}}\psi(k_z), \quad \text{(A5)}$$

where $|\omega| < |\Delta|$, and $H^{\mathrm{ind}}_{\mathrm{eff}}$ is defined as

$$H^{\mathrm{ind}}_{\mathrm{eff}}(k_z,\omega) = H_{\mathrm{SM}}(k_z) + \Sigma^{\mathrm{static}}_{\mathrm{MI}}(\Gamma=0) + \Sigma_{\mathrm{SC}}(k_z,\omega). \quad \text{(A6)}$$

Note that we have used the superscript "ind" to indicate that this energy-dependent, effective Hamiltonian is used for calculating the induced gap at $\Gamma = 0$. Also note that in Eq. (A5) ω appears both within the effective Hamiltonian and as the eigenvalue. Therefore, we must solve the eigenvalue equation self-consistently, e.g., the input ω needs to be equal to one of the eigenvalues of the effective Hamiltonian. To understand how we can find the eigenvalue ω self-consistently, we plot in Fig. 6 the lowest positive eigenvalue (red solid line) of $H^{\mathrm{ind}}_{\mathrm{eff}}(k_z,\omega)$ as a function of ω for some example system parameters with $\Gamma = 0$. Equation (A5) is satisfied when the eigenvalue curve interests the line $E = \omega$ (black dashed line). We notice that the lowest positive eigenvalue of $H^{\mathrm{ind}}_{\mathrm{eff}}(k_z,\omega)$ is monotonic over the range $0 < \omega < |\Delta|$. Therefore, a simply bisection algorithm allows us to find ω satisfying (A5), provided it exists, by iteratively reducing the subinterval in which $\omega = E_1(\omega)$ is possible, where E_1 is the lowest positive eigenvalue of the effective Hamiltonian (A6).

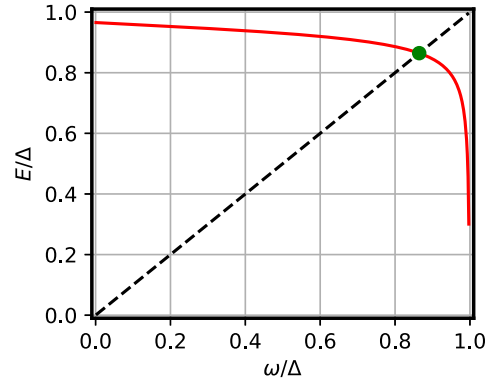

FIG. 6. The lowest positive eigenvalue (red solid line) of $H^{\mathrm{ind}}_{\mathrm{eff}}(k_z,\omega)$ is plotted as a function of input ω for some example system parameters with $\Gamma = 0$. The energy of a subgap state is found where the eigenvalue curve intersects (indicated by a green dot) the line $E = \omega$ (black dashed line).

[1] A. Stern, Non-abelian states of matter, Nature (London) **464**, 187 (2010).

[2] E. Majorana, Teoria simmetrica dell'elettrone e del positrone, Nuovo Cimento **5**, 171 (1937).

[3] A. Y. Kitaev, Unpaired Majorana fermions in quantum wires, Phys. Usp. **44**, 131 (2001).

[4] A. Kitaev, Fault-tolerant quantum computation by anyons, Ann. Phys. **303**, 2 (2003).

[5] C. Nayak, S. H. Simon, A. Stern, M. Freedman, and S. Das Sarma, Non-abelian anyons and topological quantum computation, Rev. Mod. Phys. **80**, 1083 (2008).

[6] S. Das Sarma, M. Freedman, and C. Nayak, Majorana zero modes and topological quantum computation, npj Quantum Inf. **1**, 15001 (2015).

[7] T. D. Stanescu, *Introduction to Topological Quantum Matter and Quantum Computation* (CRC, Taylor & Francis Group, Boca Raton, 2017).

[8] J. Alicea, New directions in the pursuit of Majorana fermions in solid state systems, Rep. Prog. Phys. **75**, 076501 (2012).

[9] M. Leijnse and K. Flensberg, Introduction to topological superconductivity and Majorana fermions, Semicond. Sci. Technol. **27**, 124003 (2012).

[10] T. D. Stanescu and S. Tewari, Majorana fermions in semiconductor nanowires: Fundamentals, modeling, and experiment, J. Phys.: Condens. Matter **25**, 233201 (2013).

[11] C. Beenakker, Search for Majorana fermions in superconductors, Annu. Rev. Condens. Matter Phys. **4**, 113 (2013).

[12] S. R. Elliott and M. Franz, Colloquium: Majorana fermions in nuclear, particle, and solid-state physics, Rev. Mod. Phys. **87**, 137 (2015).

[13] R. Aguado, Majorana quasiparticles in condensed matter, Riv. Nuovo Cimento **40**, 523 (2017).

[14] R. M. Lutchyn, E. P. a. M. Bakkers, L. P. Kouwenhoven, P. Krogstrup, C. M. Marcus, and Y. Oreg, Majorana zero modes in superconductor–semiconductor heterostructures, Nat. Rev. Mater. **3**, 52 (2018).

[15] L. Fu and C. L. Kane, Superconducting Proximity Effect and Majorana Fermions at the Surface of a Topological Insulator, Phys. Rev. Lett. **100**, 096407 (2008).

[16] J. D. Sau, R. M. Lutchyn, S. Tewari, and S. Das Sarma, Generic New Platform for Topological Quantum Computation Using Semiconductor Heterostructures, Phys. Rev. Lett. **104**, 040502 (2010).

[17] S. Nadj-Perge, I. K. Drozdov, B. A. Bernevig, and A. Yazdani, Proposal for realizing Majorana fermions in chains of magnetic atoms on a superconductor, Phys. Rev. B **88**, 020407(R) (2013).

[18] R. M. Lutchyn, J. D. Sau, and S. Das Sarma, Majorana Fermions and a Topological Phase Transition in Semiconductor-Superconductor Heterostructures, Phys. Rev. Lett. **105**, 077001 (2010).

[19] Y. Oreg, G. Refael, and F. von Oppen, Helical Liquids and Majorana Bound States in Quantum Wires, Phys. Rev. Lett. **105**, 177002 (2010).

[20] V. Mourik, K. Zuo, S. M. Frolov, S. R. Plissard, E. P. A. M. Bakkers, and L. P. Kouwenhoven, Signatures of Majorana fermions in hybrid superconductor-semiconductor nanowire devices, Science **336**, 1003 (2012).

[21] A. Das, Y. Ronen, Y. Most, Y. Oreg, M. Heiblum, and H. Shtrikman, Zero-bias peaks and splitting in an Al-InAs nanowire topological superconductor as a signature of Majorana fermions, Nat. Phys. **8**, 887 (2012).

[22] A. D. K. Finck, D. J. Van Harlingen, P. K. Mohseni, K. Jung, and X. Li, Anomalous Modulation of a Zero-Bias Peak in a Hybrid Nanowire-Superconductor Device, Phys. Rev. Lett. **110**, 126406 (2013).

[23] S. M. Albrecht, A. P. Higginbotham, M. Madsen, F. Kuemmeth, T. S. Jespersen, J. Nygård, P. Krogstrup, and C. M. Marcus, Exponential protection of zero modes in majorana islands, Nature (London) **531**, 206 (2016).

[24] F. Nichele, A. C. C. Drachmann, A. M. Whiticar, E. C. T. O'Farrell, H. J. Suominen, A. Fornieri, T. Wang, G. C. Gardner, C. Thomas, A. T. Hatke, P. Krogstrup, M. J. Manfra, K. Flensberg, and C. M. Marcus, Scaling of Majorana Zero-Bias Conductance Peaks, Phys. Rev. Lett. **119**, 136803 (2017).

[25] B. Nijholt and A. R. Akhmerov, Orbital effect of magnetic field on the Majorana phase diagram, Phys. Rev. B **93**, 235434 (2016).

[26] T. Karzig, C. Knapp, R. M. Lutchyn, P. Bonderson, M. B. Hastings, C. Nayak, J. Alicea, K. Flensberg, S. Plugge, Y. Oreg, C. M. Marcus, and M. H. Freedman, Scalable designs for quasiparticle-poisoning-protected topological quantum computation with Majorana zero modes, Phys. Rev. B **95**, 235305 (2017).

[27] J. D. Sau, S. Tewari, R. M. Lutchyn, T. D. Stanescu, and S. Das Sarma, Non-Abelian quantum order in spin-orbit-coupled semiconductors: Search for topological Majorana particles in solid-state systems, Phys. Rev. B **82**, 214509 (2010).

[28] S. Vaitiekėnas, Y. Liu, P. Krogstrup, and C. M. Marcus, Zero-bias peaks at zero magnetic field in ferromagnetic hybrid nanowires, Nat. Phys. **17**, 43 (2020).

[29] Y. Liu, A. Luchini, S. Martí-Sánchez, C. Koch, S. Schuwalow, S. A. Khan, T. Stankevič, S. Francoual, J. R. L. Mardegan, J. A. Krieger, V. N. Strocov, J. Stahn, C. A. F. Vaz, M. Ramakrishnan, U. Staub, K. Lefmann, G. Aeppli, J. Arbiol, and P. Krogstrup, Coherent epitaxial semiconductor–ferromagnetic insulator inas/eus interfaces: Band alignment and magnetic structure, ACS Appl. Mater. Interfaces **12**, 8780 (2020).

[30] Y. Liu, S. Vaitiekėnas, S. Martí-Sánchez, C. Koch, S. Hart, Z. Cui, T. Kanne, S. A. Khan, R. Tanta, S. Upadhyay, M. E. Cachaza, C. M. Marcus, J. Arbiol, K. A. Moler, and P. Krogstrup, Semiconductor–ferromagnetic insulator–superconductor nanowires: Stray field and exchange field, Nano Lett. **20**, 456 (2020).

[31] P. M. Tedrow, J. E. Tkaczyk, and A. Kumar, Spin-Polarized Electron Tunneling Study of an Artificially Layered Superconductor with Internal Magnetic Field: Euo-Al, Phys. Rev. Lett. **56**, 1746 (1986).

[32] T. Tokuyasu, J. A. Sauls, and D. Rainer, Proximity effect of a ferromagnetic insulator in contact with a superconductor, Phys. Rev. B **38**, 8823 (1988).

[33] F. S. Bergeret, A. F. Volkov, and K. B. Efetov, Induced ferromagnetism due to superconductivity in superconductor-ferromagnet structures, Phys. Rev. B **69**, 174504 (2004).

[34] E. Strambini, V. N. Golovach, G. De Simoni, J. S. Moodera, F. S. Bergeret, and F. Giazotto, Revealing the magnetic proximity effect in eus/al bilayers through superconducting tunneling spectroscopy, Phys. Rev. Mater. **1**, 054402 (2017).

[35] T. T. Heikkilä, M. Silaev, P. Virtanen, and F. S. Bergeret, Thermal, electric and spin transport in superconductor/ferromagnetic-insulator structures, Prog. Surf. Sci. **94**, 100540 (2019).

[36] T. D. Stanescu and S. Das Sarma, Proximity-induced low-energy renormalization in hybrid semiconductor-superconductor Majorana structures, Phys. Rev. B **96**, 014510 (2017).

[37] B. S. Chandrasekhar, A note on the maximum critical field of high-field superconductors, Appl. Phys. Lett. **1**, 7 (1962).

[38] A. M. Clogston, Upper Limit for the Critical Field in Hard Superconductors, Phys. Rev. Lett. **9**, 266 (1962).

[39] W. Chen, X. Zhang, and Y. Huang, Luminescence enhancement of eus nanoclusters in zeolite, Appl. Phys. Lett. **76**, 2328 (2000).

[40] A. E. Antipov, A. Bargerbos, G. W. Winkler, B. Bauer, E. Rossi, and R. M. Lutchyn, Effects of Gate-Induced Electric Fields on Semiconductor Majorana Nanowires, Phys. Rev. X **8**, 031041 (2018).

[41] B. D. Woods, T. D. Stanescu, and S. Das Sarma, Effective theory approach to the Schrodinger-Poisson problem in semiconductor Majorana devices, Phys. Rev. B **98**, 035428 (2018).

[42] R. M. L. Ramdas, *Finite Element and Boundary Element Applications in Quantum Mechanics* (Oxford University Press, Oxford, 2007).

[43] B. D. Woods, Majorana nanostructures and their electrostatic environment, Ph.D. thesis, West Virginia University, 2021.

[44] M. Alnaes, J. Blechta, J. Hake, A. Johansson, B. Kehlet, A. Logg, C. Richardson, J. Ring, M. Rognes, and G. Wells, The fenics project version 1.5, Arch. Num. Software **3**, 9 (2015).

[45] C. Geuzaine and J. F. Remacle, Gmsh: A three-dimensional finite element mesh generator with built-in pre- and post-processing facilities, Int. J. Numer. Methods Eng. **79**, 1309 (2009).

[46] B. D. Woods, S. Das Sarma, and T. D. Stanescu, Subband occupation in semiconductor-superconductor nanowires, Phys. Rev. B **101**, 045405 (2020).

[47] N. A. Court, A. J. Ferguson, and R. G. Clark, Energy gap measurement of nanostructured aluminium thin films for single cooper-pair devices, Supercond. Sci. Technol. **21**, 015013 (2007).

[48] W. Müller and W. Nolting, Temperature-dependent quasiparticle band structure of the ferromagnetic semiconductor eus, Phys. Rev. B **66**, 085205 (2002).

[49] M. P. L. Sancho, J. M. L. Sancho, J. M. L. Sancho, and J. Rubio, Highly convergent schemes for the calculation of bulk and surface green functions, J. Phys. F **15**, 851 (1985).

[50] J. Klimeš, Inelastic transmission of current through molecular bridge, Master's thesis, Department of Chemical Physics and Optics, Charles University of Prague, 2007.